

## Modular heat storage in waste heat recovery installations

PIOTR GÓRSZCZAK<sup>a</sup>  
MARCIN RYWOTYCKI<sup>a\*</sup>  
MARCIN HOJNY<sup>a</sup>  
GRZEGORZ FILO<sup>b</sup>

<sup>a</sup> AGH University of Krakow, Mickiewicza 30, 30-059 Kraków, Poland

<sup>b</sup> Cracow University of Technology, Jana Pawła II 37, 31-864 Kraków, Poland

**Abstract** The paper presents the methodology of designing a system for accumulating waste heat from industrial processes. The research aimed to analyse the fluid's movement in the heat accumulator to unify the temperature field in the volume of water constituting the heat buffer. Using the computer program Ansys Fluent, a series of computational fluid dynamics simulations of the process of charging the heat storage with water at 60°C, 70°C, and 80°C was carried out. The selected temperatures correspond to the temperature range of unmanaged waste heat. In the presented solution, heat storage is loaded with water from the cooling systems of industrial equipment to store excess heat and use it at a later time. The results of numerical calculations were used to analyse the velocity and temperature fields in the selected structure of the modular heat storage. A novelty in the presented solution is the use of smaller modular heat storage units that allow any configuration of the heat storage system. This solution makes it possible to create heat storage with the required heat capacity.

**Keywords:** Heat storage; Heat recovery; Waste heat, CFD

### Nomenclature

$C_{1\epsilon}$ , $C_{2\epsilon}$ , $C_{\mu}$	–	turbulence model constants
$c$	–	specific heat, $\text{J kg}^{-1}\text{K}^{-1}$
$G_k$	–	generating kinetic energy of turbulence

---

\*Corresponding Author. Email: [rywotyc@agh.edu.pl](mailto:rywotyc@agh.edu.pl)

$k$	–	kinetic energy of turbulence
$p$	–	pressure, Pa
$S$	–	modulus of the average strain rate tensor
$S_{ij}$	–	strain rate tensor
$T$	–	temperature, K
$t$	–	time, s
$u_i, u_j, u_l$	–	velocity components, $\text{m s}^{-1}$
$x_i, x_j, x_l$	–	Cartesian coordinates, m

### Greek symbols

$\delta_{ij}$	–	Kronecker delta
$\epsilon$	–	dissipation coefficient
$\lambda$	–	heat conductivity, $\text{W m}^{-1}\text{K}^{-1}$
$\mu$	–	dynamic viscosity coefficient, $\text{kg m}^{-1}\text{s}^{-1}$
$\mu_t$	–	turbulent viscosity, $\text{m}^2\text{s}^{-1}$
$\rho$	–	density, $\text{kg m}^{-3}$
$\sigma_k$	–	turbulent Prandtl number for $k$
$\sigma_\epsilon$	–	turbulent Prandtl number for $\epsilon$

## 1 Introduction

Thermal energy is a by-product of every energy generation and industrial process. The growing crisis and rising environmental problems force the development of heat recovery systems to mitigate the current situation [1]. Waste heat recovery is one of the most promising ways to improve the energy efficiency of many technological processes and energy devices [2]. All kinds of construction industries are among the most energy-intensive areas. This sector accounts for almost a third of the world's total energy consumption. Domestic hot water, space heating and cooling currently account for about 50% of energy consumption in the construction sector [3]. Thanks to waste heat recovery systems, it will be possible to reduce CO<sub>2</sub> emissions, and fossil fuel consumption [4]. Nowadays, all countries around the World are in a period of energy transformation. Distributed energy, complementary to fossil and renewable energy, is currently a research hotspot. However, the variability and discontinuity of renewable energy require the use of energy storage facilities that will provide energy in the event of insufficient production from renewable energy sources (RES) [5]. Numerous industrial processes generate a significant amount of low-temperature waste heat, a potential source for building heating systems and industries such as drying, pasteurization, water heating and distillation in the paper, food, tobacco, wood, etc., chemical and machinery sectors. A low-temperature heat

source could be sufficient to heat buildings; however, high-temperature water, steam or air is required in the abovementioned industrial branches. This temperature can be achieved by using electric heating or traditional fossil fuel boilers. This is associated with low energy efficiency and high emission of pollutants into the atmosphere. To improve energy efficiency, traditional boilers can be replaced by heat pumps, a more efficient method of high-temperature heating. When generating energy in a heat pump, no production of pollutants could get into the atmosphere [6]. However, waste heat production does not always correlate with actual heat demand. This makes it necessary to accumulate this heat and use it at a later time. Therefore, one of the most urgent issues in the power industry is collecting and storing the generated thermal energy using heat accumulators. Such devices can be used as thermal power reserves during night hours or system failures [7]. In addition, thermal energy can be converted into electrical energy for production in the thermomechanical cycle when there is a demand for it [8]. The modular heat storage is usually a few hundred litres, well-insulated accumulator tank that allows heat to be stored in the form of, for example, hot water. The heat source can be water from industrial equipment's cooling systems. Due to the risk of evaporation, heat storage with water is mainly used at temperatures below 90°C [9,10]. The dynamic and static modes can be distinguished during the water tank operation. The dynamic mode of operation refers to the process of loading and unloading the water tank. The static operating mode refers to the thermal behaviour of the heat storage when water is accumulated [11]. If necessary, the accumulated heat can be transferred at a given time and in a certain amount to various receivers in the building, such as radiators, floor heating or domestic hot water (DHW) storage heaters [12]. Unused heat should be managed for its subsequent use in low-temperature processes and heating buildings. A diagram of such an installation is shown in Fig. 1.

In such an example installation, the heating fluid operates in a closed circuit. The heated fluid flows from the waste heat source to a 4-way valve with a thermometer and, depending on the temperature, is either transferred directly to the heat consumer or heats the water in the tank thermal energy storage (TTES) for later use. An expansion vessel is used in the system and in the TTES itself to collect the excess fluid created by temperature expansion. Sensors are used throughout the system to measure the temperature of the medium.

In the literature, the static mode of operation is also called the cooling process because, due to heat loss to the environment, a natural water cool-

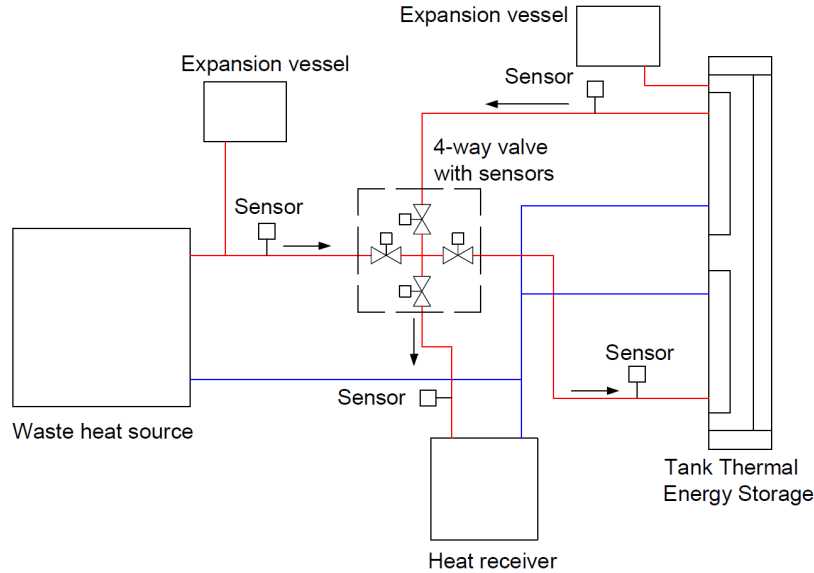


Figure 1: Scheme of waste heat storage installation.

ing process occurs [11,13]. Heat exchange between the fluid in the tank and the environment results in the creation of boundary layers of temperature and water velocity along the side wall of the tank. As a consequence of this phenomenon, thermal stratification is formed in the reservoir. This stratification significantly affects the capacity of the accumulated thermal energy and even the efficiency of the entire system [11,14]. Heat storage, also called accumulation, is present in heat accumulators, i.e., thermal energy storage (TES). Depending on the temperature of the storage medium, heat accumulation can be divided into low-temperature, whose temperature does not exceed  $120^{\circ}\text{C}$ , medium-temperature, ranging from  $120^{\circ}\text{C}$  to  $500^{\circ}\text{C}$  [15] and high-temperature, whose temperature exceeds  $500^{\circ}\text{C}$ . In thermal energy storage, heat can be accumulated using specific heat, phase-change material (PCM), and heat of chemical transformations [16,17]. Due to their construction, heat accumulators can be divided into two main groups. The first one includes underground thermal energy storage (UTES), i.e., underground heat reservoirs that use soil, water or gravel as a storage medium. The second form of storage is a water reservoir, i.e., tank thermal energy storage (TTES) [16]. In general, the energy storage density of overt heat storage materials is relatively low (in the range of approximately 10 to  $50\text{ kWh m}^{-3}$  [9,18]), requiring more materials and larger tanks [9,19].

Heat storage with very large capacities are used in power plants [20]. This arrangement feeding the district heating system. Such solutions are applicable to areas with access to the district heating system [21].

A novelty in the presented solution is the use of smaller modular heat storage units that permit any configuration of the heat storage system and the use of thicker insulation than in standard tanks, which results in lower heat losses to the environment. The proposed solution makes it possible to create heat storage with the required heat capacity. Particularly, this work provides an analysis of heat storage accumulating heat in an overt form up to 80°C. A series of computational fluid dynamics (CFD) simulations of the TTES charging process with water at 60°C, 70°C, and 80°C were carried out. The research demonstrates the influence of the temperature and the tank's structure on the movement of the water velocity field in the tank and heat loss as a result of heat conduction through its walls. In the literature, one can find various uses of thermal energy storage with phase change substance, which accumulate waste heat and heat from solar energy [22, 23]. Phase change materials have a high heat capacity but only in a narrow temperature range, while water works better in a broader scope. Phase change material (PCM) is also much more expensive than commonly available water. Due to the low interest in the area of modular TTES loaded with water from waste heat recovery installations and the matter of extending the ranges of applied temperatures, the presented publication fills this gap.

## 2 Methodology: computational fluid dynamics method

Effective modelling of the charging process of modular heat storage requires the use of mathematical models that allow the determination of the temperature field and the velocity field resulting from water heating in the tank. The heated water temperature field results from two heat transport mechanisms, convection and conduction. The conduction equation with a convection term, also known as the Fourier-Kirchhoff equation, can describe their mutual overlap. The general form of this equation is [24, 25]

$$\frac{\partial T}{\partial t} + u_i \frac{\partial T}{\partial x_i} + u_j \frac{\partial T}{\partial x_j} + u_l \frac{\partial T}{\partial x_l} = \frac{\lambda}{c\rho} \left( \frac{\partial^2 T}{\partial x_i^2} + \frac{\partial^2 T}{\partial x_j^2} + \frac{\partial^2 T}{\partial x_l^2} \right). \quad (1)$$

The Navier-Stokes equation coupled with continuity equation, describes the heated water velocity field. The general form of this equation, describing the movement of a viscous fluid, is as follows [26]:

$$\frac{\partial}{\partial t}(\rho u_i) + \frac{\partial}{\partial x_j}(\rho u_i u_j) = \rho g_i - \frac{\partial p}{\partial x_i} + \frac{\partial}{\partial x_j} \left[ \mu \left( \frac{\partial u_i}{\partial x_j} + \frac{\partial u_j}{\partial x_i} - \frac{2}{3} \delta_{ij} \frac{\partial u_l}{\partial x_l} \right) \right], \quad (2)$$

$$\frac{\partial \rho}{\partial t} + \frac{\partial}{\partial x_i}(\rho u_i) = 0. \quad (3)$$

Turbulent flow is a three-dimensional, non-constant, random motion observed in fluids at moderate to high Reynolds numbers above 3600 [26]. Since technical flows are usually based on low-viscosity fluids, almost all are turbulent. Many technically essential quantities, such as the mixing of momentum, energy, and substance kinds, heat transfer, pressure losses and efficiency, depend on turbulence. Turbulent flows are unsteady, and their accurate simulation requires high computing power. For this reason, averaging methods must be applied to the Navier-Stokes equations to filter out all, or at least, parts of the turbulence spectrum. The most widely used solution is trying to solve the time-averaged equations of motion for fluid flow – the Reynolds-averaged Navier-Stokes (RANS) equations. This process eliminates all turbulent structures from the flow, and a smooth change of the averaged velocity and pressure fields can be obtained. However, the averaging process introduces additional unknowns into the transport equations that need to be related to the averages somehow, which is why the so-called turbulence modelling occurs at this stage [27, 28]. The quality of the simulation may depend on the turbulence model selected. It is essential to choose a suitable model and provide the appropriate numerical mesh for the selected model. An alternative to RANS constitutes the scale-resolving simulation (SRS) model. In SRS methods, at least part of the turbulence spectrum is resolved in at least part of the flow domain. The best-known method is large eddy simulation (LES); however, many new hybrids (models between RANS and LES) are emerging. Since all SRS methods require timed simulations where the time step is relatively small, it is crucial to understand that these methods are computationally much more demanding than RANS simulations. The RANS models include the Spalart-Allmaras model,  $k-\epsilon$ ,  $k-\omega$ , and Reynold's stress. The  $k-\epsilon$  model belongs to the family of time-averaged Navier-Stokes (RANS) turbulence models in which all turbulence effects are modelled. It is a model based on two equations [29]. This

means that in addition to conservation equations, it also solves two transport equations, such as convection and diffusion of turbulent energy [30]. The standard  $k$ - $\epsilon$  model is a semi-empirical model based on default transport equations for turbulence kinetic energy,  $k$ , and its dissipation coefficient,  $\epsilon$ . Both variables contribute to the turbulent viscosity,  $\mu_t$ . It is designed to model the apparent increase in viscosity associated with the existence of additional fluctuations. In this case, the transport equations may be written as follows:

$$\frac{\partial u_i}{\partial t} + u_j \frac{\partial u_i}{\partial x_j} = \rho g_i - \frac{1}{\rho} \frac{\partial p}{\partial x_i} - \frac{1}{\rho} \frac{\partial}{\partial x_j} \left[ (\mu + \mu_t) \left( \frac{\partial u_i}{\partial x_j} + \frac{\partial u_j}{\partial x_i} \right) \right], \quad (4)$$

$$\frac{\partial u_j}{\partial x_j} = 0, \quad (5)$$

$$\frac{\partial(\rho k)}{\partial t} + \frac{\partial(\rho k u_j)}{\partial x_j} = \frac{\partial}{\partial x_j} \left[ \left( \mu + \frac{\mu_t}{\sigma_k} \right) \frac{\partial k}{\partial x_j} \right] + G_k - \rho \epsilon, \quad (6)$$

$$\frac{\partial(\rho \epsilon)}{\partial t} + \frac{\partial(\rho \epsilon u_j)}{\partial x_j} = \frac{\partial}{\partial x_j} \left[ \left( \mu + \frac{\mu_t}{\sigma_\epsilon} \right) \frac{\partial \epsilon}{\partial x_j} \right] + C_{1\epsilon} G_k \frac{\epsilon}{k} - C_{2\epsilon} \rho \frac{\epsilon^2}{k}. \quad (7)$$

The transport equations for  $k$  and  $\epsilon$  include additional quantities such as:

$$\mu_t = \rho C_\mu \frac{k^2}{\epsilon}, \quad G_k = \mu_t S^2, \quad S = \sqrt{2S_{ij}S_{ij}}, \quad S_{ij} = \frac{1}{2} \left( \frac{\partial u_i}{\partial x_j} + \frac{\partial u_j}{\partial x_i} \right).$$

The model also requires several constants. In the carried out research, by the general Ansys/Fluent recommendations [31], they amounted to:

$$C_\mu = 0.09, \quad C_{1\epsilon} = 1.44, \quad C_{2\epsilon} = 1.92, \quad \sigma_k = 1.0, \quad \sigma_\epsilon = 1.3.$$

Equations (4) and (5) are valid only for incompressible flows. The tested working medium is water, which is treated as an incompressible fluid. For this reason, the over mentioned equations are appropriate. The formulated equations are solvable for averaged values over a suitable time period. It is assumed that the averaged values may still vary over time to some extent [28]. In the derivation of the  $k$ - $\epsilon$  model, it was assumed that the flow is turbulent since the standard  $k$ - $\epsilon$  model is valid for fully turbulent flows [27]. Finally, based on the Ansys Fluent documentation [27,31], among many different mathematical models, the  $k$ - $\epsilon$  turbulence model was used mainly due to optimal calculation time and high stability.

### 3 Case study: numerical model

Calculations of the heat capacity of a single tank were carried out for different charging temperatures. It was assumed to build compact heat storage with internal dimensions of  $2.0 \text{ m} \times 0.5 \text{ m} \times 0.5 \text{ m}$ , which was filled with water. The actual volume of stored medium is therefore  $0.472 \text{ m}^3$ . This is the volume calculated with Ansys DesignModeler on the basis of the geometry after subtracting the heating and heat-receiving plates, which is filled with water. The initial temperature of the water in the tank was assumed to be  $12^\circ\text{C}$ , and the final temperatures amounted to  $60^\circ\text{C}$ ,  $70^\circ\text{C}$ , and  $80^\circ\text{C}$ , respectively. The accumulator heat capacity was determined based on the energy balance. The specific heat of the water and the temperature difference were used to calculate the heat capacity. The calculated heat capacity at different charging temperatures converted to kWh is presented in Table 1.

Table 1: Summary of thermal capacity for different charging temperatures.

Charging temperature ( $^\circ\text{C}$ )	Heat capacity (kWh)
60	26.27
70	31.78
80	37.32

The tank geometry (Fig. 2) was created in DesignModeler, which is part of the Ansys package 2022 R2 [32]. The buffer consists of a steel sheet tank which thickness is  $0.005 \text{ m}$ , polystyrene insulation which thickness is  $0.1 \text{ m}$ ,

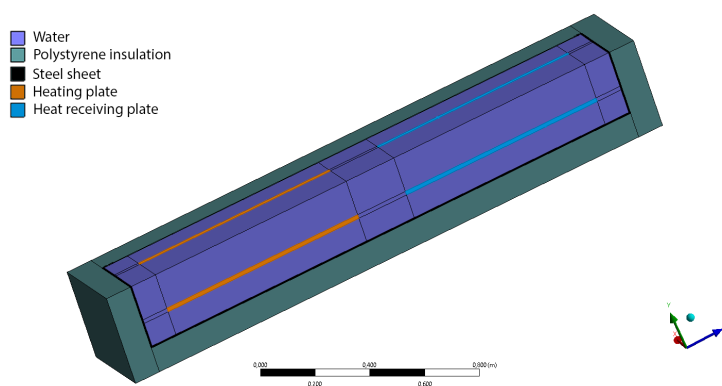


Figure 2: Tank geometry created in DesignModeler.

a copper heating plate, and a heat receiving plate which length is 0.8 m, while the width is 0.015 m. To speed up numerical calculations, symmetry was used when creating the geometry, which reduced the number of mesh elements. The external dimensions of the tank, after taking into account symmetry, are 2.21 m in height and 0.355 m in width.

Two types of model meshing methods were proposed: automatic and MultiZone. The automatic method is the default mesh generation method in Ansys Meshing. This method attempts to sweep the mesh for solid (3D) models and generate quadrilateral elements for surface solid (2D) models. Sweep mesh generates a mesh on one surface (the source surface) of the body and literally ‘sweeps’ along the body to another surface (the target surface). The mesh pattern is identical along the entire length of the body. The MultiZone mesh method automatically decomposes geometry into mapped regions (structured/stretched) and free regions (unstructured). Where possible, it automatically generates a clean cubic mesh, then fills the harder-to-grasp areas with an unstructured mesh [27,32].

Two methods, automatic and MultiZone, were used when creating the mesh on the tank model. The automatically created mesh used in the calculation is shown in Fig. 3 and has 1 523 617 elements. This method is characterized by the fact that the program selects the optimal geometry structure itself. The minimum orthogonal quality of this mesh is 0.1, and the maximum quality is 0.99. The average mesh quality is 0.77. The average skewness of the elements is 0.23. The size of mesh elements is 0.04 m. Local refinement was used in the areas where water meets solid surfaces.

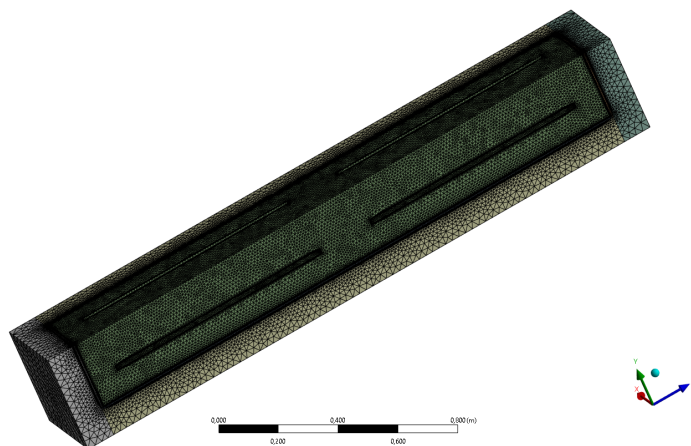


Figure 3: Tank mesh created in Ansys Meshing using automatic algorithm.

For comparison, the mesh created with the help of the MultiZone method is shown in Fig. 4 and has 665 724 elements. The minimum mesh quality is 0.58, and the maximum mesh quality is 1.00, with an average value of 0.99. The average skewness of the elements is 0.03, and the size of mesh elements is 0.008 m. The MultiZone method was used to create a mesh of the fluid body in order to obtain a hexagonal shape. Local mesh refinement was applied in the areas where water meets surfaces.

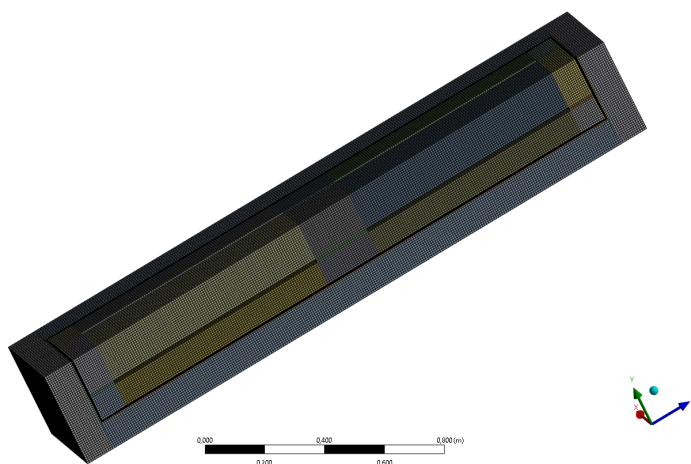


Figure 4: Tank mesh created in Ansys Meshing with the MultiZone method.

The most commonly used indicators characterizing a given mesh are skewness and orthogonal quality. Ansys recommends the minimum orthogonal quality to be higher than 0.1 and the maximum skewness less than 0.95. These values are acceptable, but the higher the minimum orthogonal quality and the lower the maximum skewness, the more reliable results can be obtained from subsequent CFD simulations [33]. Comparing the above two meshes (Figs. 3 and 4) and recommendations, it can be seen that thanks to the use of the MultiZone method, the quality is excellent. In the case of the automatic method, it is also acceptable, but its parameters are noticeably worse. In Ansys Fluent, appropriate physical properties were assigned to individual materials presented in Table 2. An initial boundary condition was assigned to each wall of the tank. For external walls (insulation) temperature of 15°C and a heat transfer coefficient of 15 Wm<sup>-2</sup>K<sup>-1</sup> were set. System coupling was assigned to the internal walls (sheet metal) and to the heat-receiving plate. The hotplate was ascribed an initial temperature of

60°C, 70°C, and 80°C. All surfaces were assigned a wall boundary condition. The Standard  $k$ - $\epsilon$  model was used as the viscosity model in the calculations to simulate the average flow characteristics under turbulent flow conditions. Pressure-velocity coupling was used to derive an additional pressure condition. The pressure-based solver allows the flow problem to be solved separately or in combination. The calculations use the simple method solution, which means that the algorithm uses the relationship between velocity and pressure corrections to enforce mass conservation and obtain a pressure field. This is the default setting for transient simulations [27]. The computation time was 10 800 s of real process time. While loading the tank with hot water, a constant temperature was set on the surface of the bottom plate responsible for heating the system. The top plate was assigned an initial temperature of the water.

Table 2: Physical properties of materials used in calculations [31].

Material type	Specific heat (Jkg <sup>-1</sup> K <sup>-1</sup> )	Density (kgm <sup>-3</sup> )	Heat conductivity (Wm <sup>-1</sup> K <sup>-1</sup> )	Dynamic viscosity (kgm <sup>-1</sup> s <sup>-1</sup> )
EPS	1210	29.933	0.033	–
Copper	381	8978	387.6	–
Steel	502.48	8030	16.27	–
Water	4182	$-0.4589T + 1129.6$	0.6	0.001

To determine the impact of the mesh quality on the accuracy of the results of numerical calculations, the results obtained using two types of meshes were compared. Figures 5–7 show the distributions of the water velocity field for the automatically-generated mesh and a mesh created using the MultiZone method. The comparisons are presented in particular time periods, at charging temperatures up to 60°C.

Analysis of Figs. 5–7 shows that the usage of automatic method leads to the accumulation of higher velocities in the upper part of the tank. The maximum velocities are observed near the plate that does not transfer heat to the system. This movement does not come from the lower heating plate, unlike the MultiZone method. In the case of the MultiZone simulation, the water velocity distribution range is smaller but uniform throughout the volume of the tank. This is related to better mesh quality; therefore, the MultiZone model is selected for further calculations.

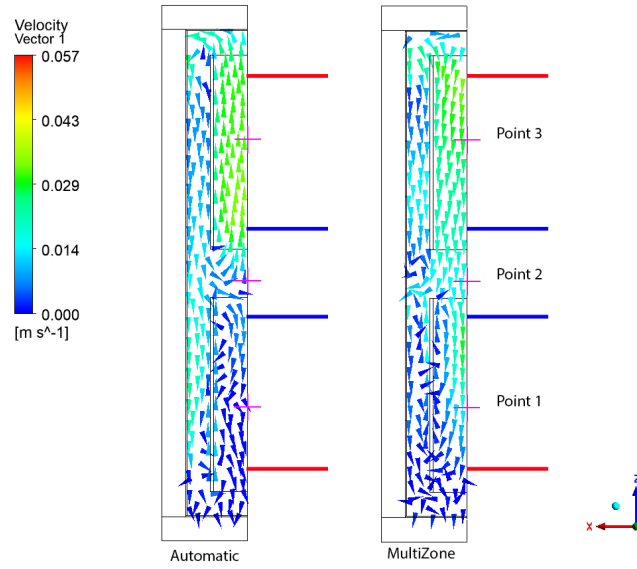


Figure 5: Distribution of water velocity in the tank after the first hour of calculations.

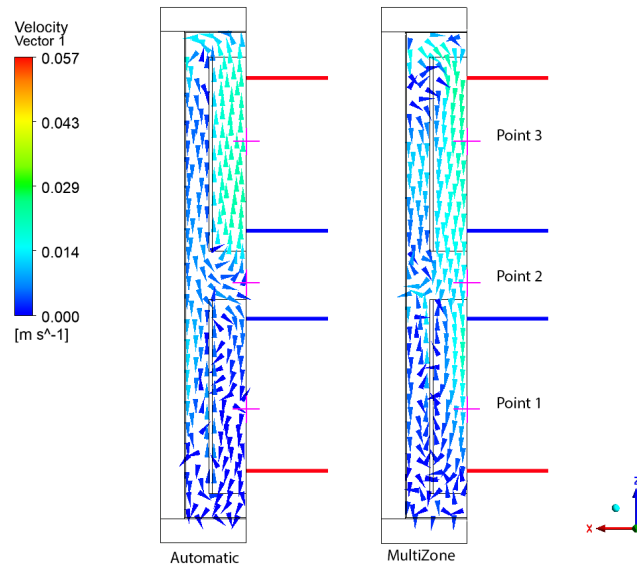


Figure 6: Distribution of water velocity in the tank after the second hour of calculations.

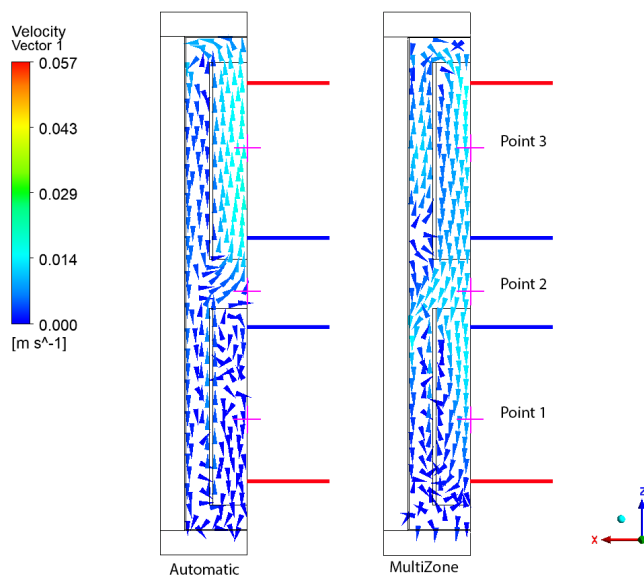


Figure 7: Distribution of water velocity in the tank after the third hour of calculations.

## 4 Computational fluid dynamics simulations and analysis of the results

Figures 8, 12, and 16 show the temperature distribution in the graphical form over the first, second and third hours when heating water in a tank with different required temperatures. Three points were distinguished in each figure mentioned above. Graphs of temperature distribution over time were prepared for each marked point, as shown in Figs. 9, 13, and 17. In addition, Figs. 10, 14, and 18 deliver the water velocity field in the tank as a result of temperature changes. Similarly, points were marked in the figures, and diagrams of the water velocity field distribution in time were made for them, which are presented in Figs. 11, 15, and 19. The Reynolds number was determined for the sections corresponding to points 1, 2, and 3 at the time moments, which are shown in Figs. 10, 14, and 18. The value is in the range of 3745–12 679, which corresponds to a fully turbulent flow ( $Re > 3600$ ) [26].

In Figs. 8 and 9 at 60°C, one can see that the temperature increases with the charging time. Similarly, Figs. 12, 13 as well as Figs. 16 and 17

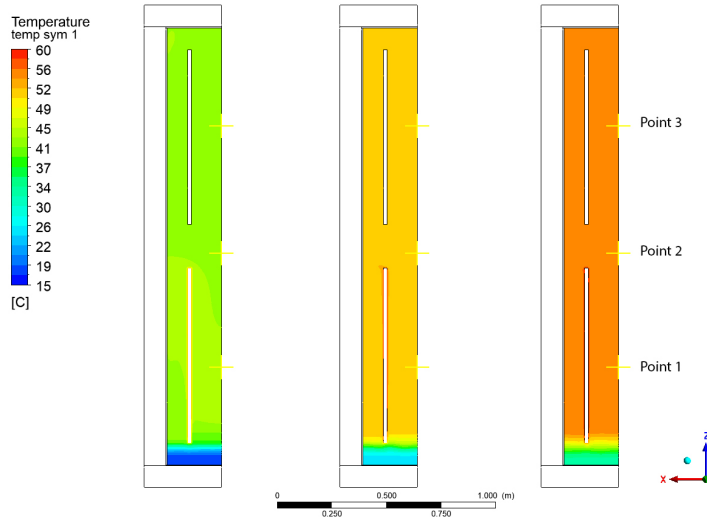


Figure 8: Temperature distribution in the tank for the maximum value of 60°C.

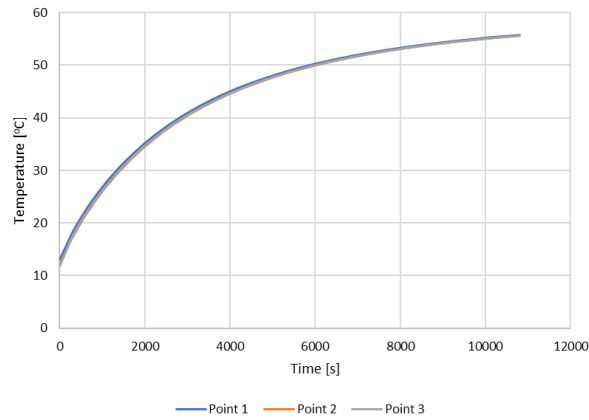


Figure 9: Graph of temperature distribution over time for a maximum value of 60°C.

refer to the temperature of 70°C and 80°C, respectively. A higher charging temperature leads to more heat stored in the warehouse and a longer discharge time. In the drawings showing the distribution of the temperature field, it can be observed that in each charging variant, there is a layer of cooler water at the bottom of the tank. This is due to the fact that the heating plate does not adhere to the bottom wall of the heat storage, so there is no global fluid movement there.

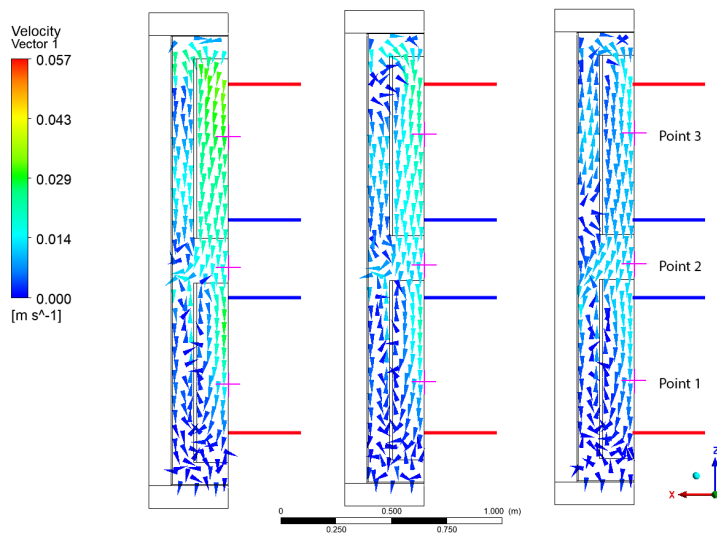


Figure 10: Water velocity distribution in the tank for the maximum temperature of 60°C.

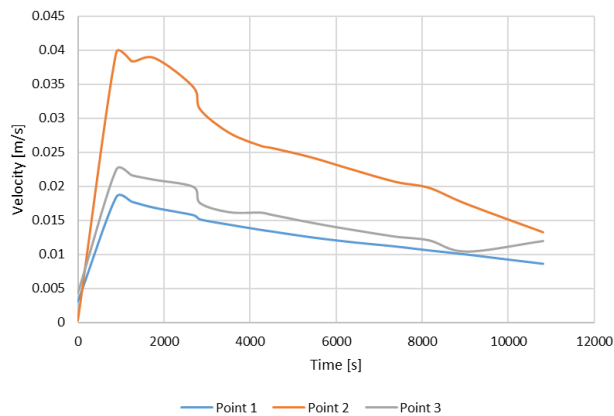


Figure 11: Graph of water velocity distribution over time for a maximum temperature of 60°C.

Figures 10, 14, and 18 show the distribution of water velocity in the tank. It can be observed that the velocity field in the upper area of the tank is significantly larger than the velocity field in the lower part. Generally, the values of the water velocity field in the entire tank are small and are caused only by the dissimilarity in water temperature resulting in its different density. Hence, it can be seen that in the tank's lower part, the fluid's

movement is negligible, which is why the temperature rises much more slowly.

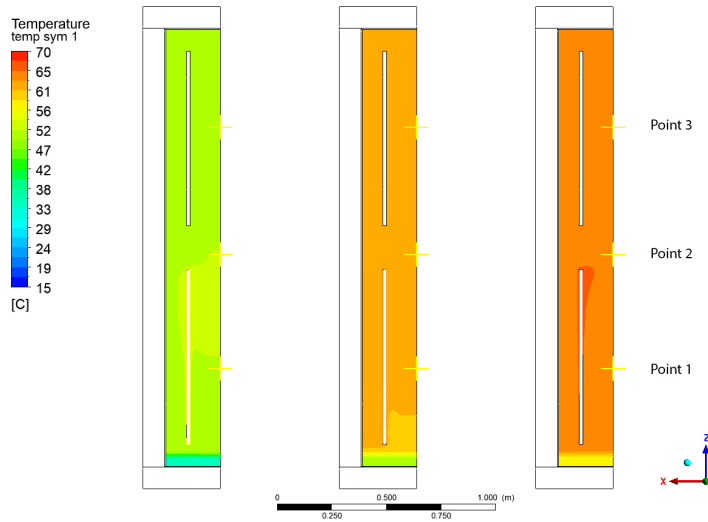


Figure 12: Temperature distribution in the tank for the maximum value of  $70^{\circ}\text{C}$ .

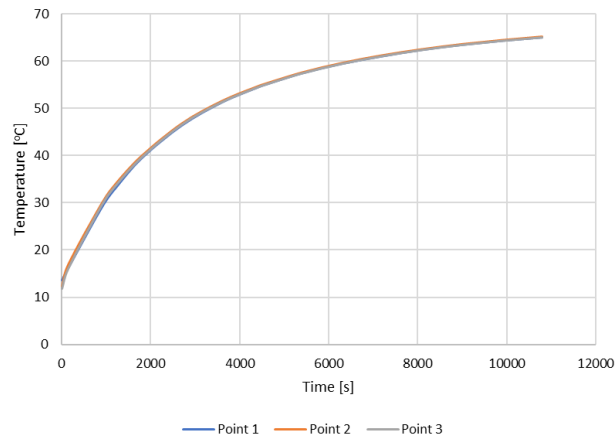


Figure 13: Graph of temperature distribution over time for a maximum value of  $70^{\circ}\text{C}$ .

Figures 11, 15, and 19 show graphs of water velocity distribution in the reservoir. In the charts, you can see an increase in speed in the initial seconds of loading. A high gradient between the initial water temperature

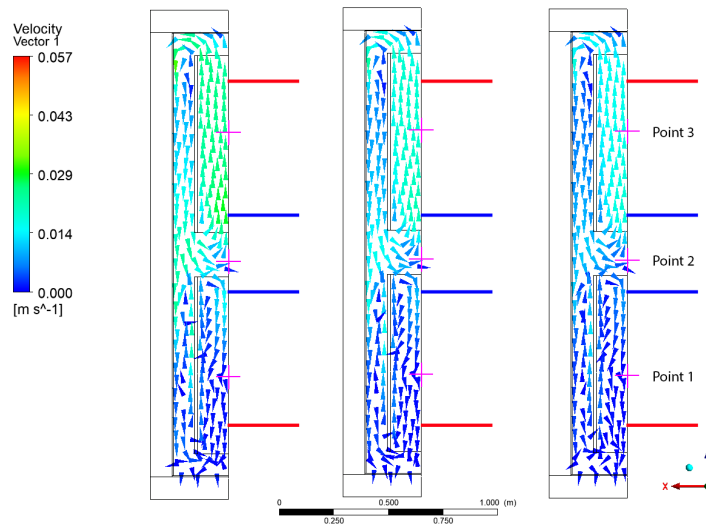


Figure 14: Water velocity distribution in the tank for the maximum temperature of 70°C.

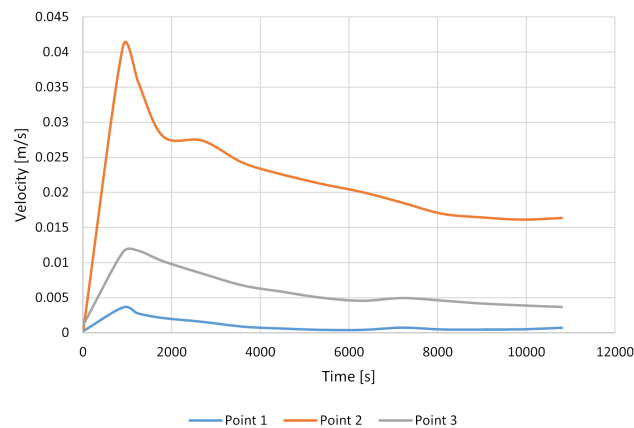


Figure 15: Water velocity distribution over time for a maximum temperature of 70°C in points 1, 2, and 3.

and the temperature of the heater causes this phenomenon. Over time, the speed starts to decrease as the temperature difference drops. In addition, the highest rate is present in the centre of the tank (point 2) since this point is close to the upper part of the heating plate. The lowest water velocity field is near the bottom of the tank (point 1) due to the faster temperature equalization.

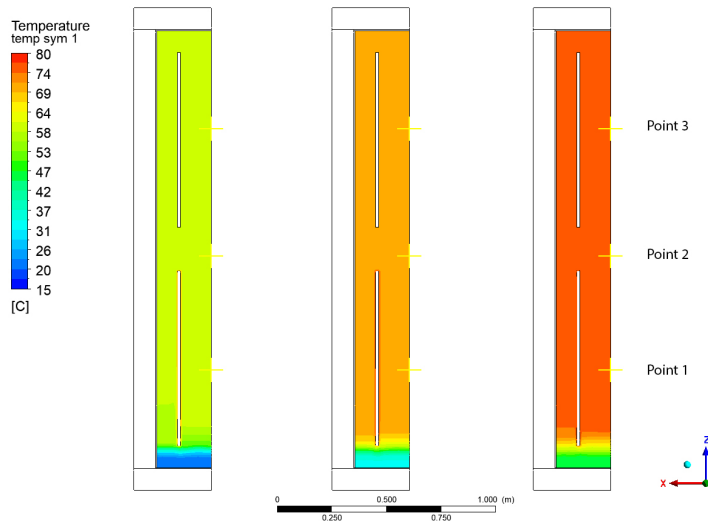


Figure 16: Temperature distribution in the tank for the maximum value of  $80^{\circ}\text{C}$ .

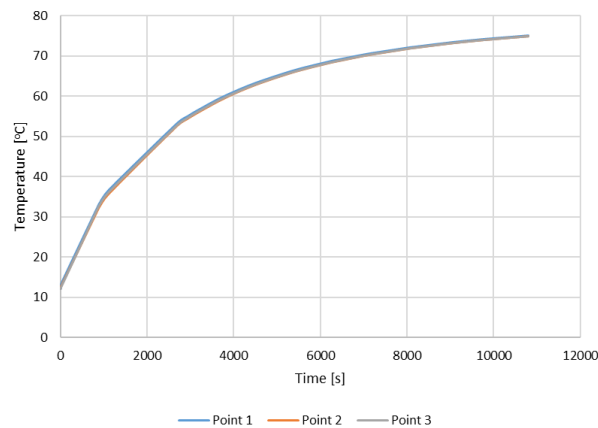


Figure 17: Graph of temperature distribution over time for a maximum value of  $80^{\circ}\text{C}$ .

From Figs. 11, 15, and 19, one can see the noticeable change in the velocity of the three points over time. The same cannot be observed for Figs. 9, 13, and 17. Temperature variation over time is still present; however, the values at each point are not significantly different. This is due to the movement of the fluid, which results in equalizing the temperature throughout the entire volume of the tank.

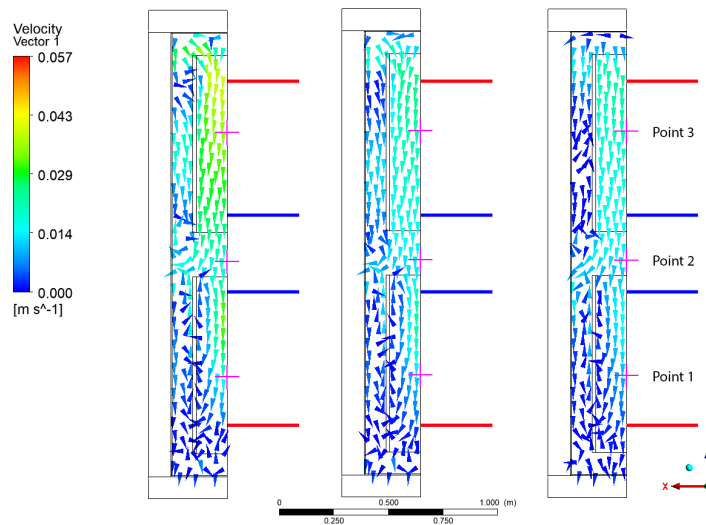


Figure 18: Water velocity distribution in the tank for the maximum temperature of 80°C.

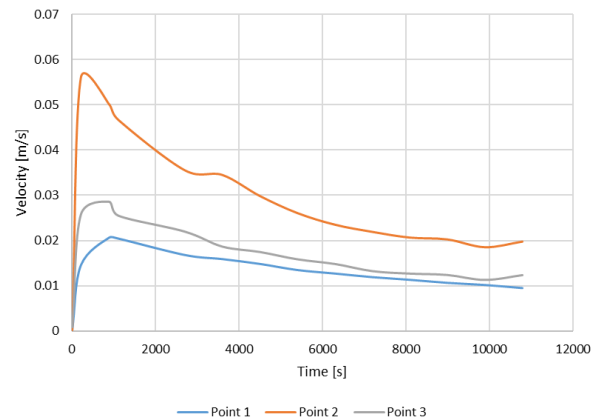


Figure 19: Water velocity distribution over time for a maximum temperature of 80°C in points 1, 2, and 3.

## 5 Total heat loss to the environment

In the calculations, expanded polystyrene (EPS) was used as the default insulation of the tank. It is a commonly used insulation material with a thermal conductivity  $0.033 \text{ Wm}^{-1}\text{K}^{-1}$ . Thanks to the applied layer of expanded polystyrene with a thickness of 0.1 m, it was possible to reduce heat losses

to the environment significantly. Table 3 shows the daily heat losses and the heat capacity of the tank at different charging temperatures and their percentage ratio. It can be read from the table that an increase in the charging temperature by 20°C causes the total heat loss to the environment increases from 1.58 to 2.33 kWh per day. However, a higher charging temperature provides more heat available to use and a longer discharge time.

Table 3: Summary of daily losses and thermal capacity of the tank.

Temperature (°C)	Daily losses (kWh)	Thermal capacity (kWh)	Percentage ratio
60	1.58	26.27	6.01
70	2.02	31.78	6.36
80	2.33	37.32	6.24

Based on Table 3, it can be concluded that the ratio of daily heat losses to the heat capacity of the tank is highly comparable depending on the charging temperature. The use of better insulation would result in a reduction of heat loss to the environment. The usage of more tanks with better insulation could meet the heat demand on unfavourable days, where direct waste heat recovery would not meet the needs.

## 6 Conclusions

- The conducted research analysed the thermal parameters of the designed compact heat storage. The study aimed to examine the movement of the fluid in such a heat accumulator to unify the temperature field in the volume of water constituting the heat buffer. Using CFD simulations, water movement in the tank was studied.
- During the tests, the heat capacity of a tank was determined, and the heat losses to the environment at different charging temperatures were estimated. Three temperatures were selected, and the heat storage was loaded into each for an equal period of time.
- In conclusion, as it arises from the results of the calculations presented in the work heating the water in the tank to 60°C is the most energy efficient, because heat losses to the environment, in this case, are the lowest.

- Due to the fact that waste heat from industrial equipment has different temperatures, such a tank will also be charged with different temperatures. Therefore, using water as an accumulation medium instead of a variable-phase substance is less expensive.
- Due to the compactness of the designed system, it can be used in various configurations depending on the environment in which it works.

## Acknowledgments

This work was supported by statutory activities of the Faculty of Metals Engineering and Industrial Computer Science of AGH University of Science and Technology, work no. 16.16.110.663 task 4.

*Received 14 June 2023*

## References

- [1] Saini M.C., Jakhar D.O.: *CFD simulation and experimental validation of PCM thermal energy storage system for micro trigeneration system application*. Int. J. Refrig. **149**(2023), 119–134. doi: [10.1016/j.ijrefrig.2022.12.004](https://doi.org/10.1016/j.ijrefrig.2022.12.004)
- [2] Fernández-Yáñez P., Romero V., Armas O., Cerretti G.: *Thermal management of thermoelectric generators for waste energy recovery*. Appl. Therm. Eng. **196**(2021), 117291. doi: [10.1016/j.applthermaleng.2021.117291](https://doi.org/10.1016/j.applthermaleng.2021.117291)
- [3] Chu S., Sethuvenkatraman S., Goldsworthy M., Yuan G.: *Techno-economic assessment of solar assisted precinct level heating systems with seasonal heat storage for Australian cities*. Renew. Energ. **201**(2022), 841–853. doi: [10.1016/j.renene.2022.11.011](https://doi.org/10.1016/j.renene.2022.11.011)
- [4] Tohidi F., Ghazanfari Holagh S., Chitsaz, A.: *Thermoelectric generators: A comprehensive review of characteristics and applications*. Appl. Therm. Eng. **201**(2021), 117793. doi: [10.1016/j.applthermaleng.2021.117793](https://doi.org/10.1016/j.applthermaleng.2021.117793)
- [5] Wang C., Wang S., Cheng X., Zhang Y., Wang, Z.: *Research progress and performance improvement of phase change heat accumulators*. J. Energ. Stor. **56**(2022), 105884. doi: [10.1016/j.est.2022.105884](https://doi.org/10.1016/j.est.2022.105884)
- [6] Dai B., Liu C., Liu S., Wang D., Wang Q., Zou T., Zhou X.: *Life cycle techno-enviro-economic assessment of dual-temperature evaporation transcritical CO<sub>2</sub> high-temperature heat pump systems for industrial waste heat recovery*. Appl. Therm. Eng. **219**(2023), 119570. doi: [10.1016/j.applthermaleng.2022.119570](https://doi.org/10.1016/j.applthermaleng.2022.119570)
- [7] Dmitry S., Liubov S.: *Numerical modelling of heat accumulator performance at storage of solar energy*. Int. J. Thermofluids **17**(2023), 100268. doi: [10.1016/j.ijft.2022.100268](https://doi.org/10.1016/j.ijft.2022.100268)

- [8] Ouyang T., Qin P., Tan X., Wang J., Fan J.: *A novel peak shaving framework for coal-fired power plant in isolated microgrids: Combined flexible energy storage and waste heat recovery*. J. Clean. Prod. **374**(2022), 133936. doi: [10.1016/j.jclepro.2022.133936](https://doi.org/10.1016/j.jclepro.2022.133936)
- [9] Fan M., Wang J., Kong X., Suo H., Zheng W., Li H.: *Experimental evaluation of the cascaded energy storage radiator for constructing indoor thermal environment in winter*. Appl. Energ. **332**(2023), 120503. doi: [10.1016/j.apenergy.2022.120503](https://doi.org/10.1016/j.apenergy.2022.120503)
- [10] Hailiot D., Lalau Y., Franquet E., Rigal S., Jay F., Bédécarrats J.P.: *A latent heat storage system for low-temperature applications: From materials selection to prototype performances*. Appl. Sci. **11**(2021), 10350. doi: [10.3390/app112110350](https://doi.org/10.3390/app112110350)
- [11] Bouhal T., ed. Dîn Fertahi S., Agrouaz Y., El Rhafiki T., Zeraouli Y., Jamil A.: *Towards an energy efficiency optimization of solar horizontal storage tanks and circulation pipes integrating evacuated tube collectors through CFD parametric studies*. Sustain. Energy Technol. Assess. **26**(2018), 93–104. doi: [10.1016/j.seta.2017.10.004](https://doi.org/10.1016/j.seta.2017.10.004)
- [12] *Heat accumulator – a way to reduce home heating costs* (in Polish). <https://muratorodom.pl/instalacje/ogrzewanie-paliwami-stalymi/akumulator-ciepla-sposob-na-obnizenie-kosztow-ogrzewania-domu-aa-EdFw-ydbp-5P5q.html> (accessed 3 Feb. 2023).
- [13] Agrouaz Y., Bouhal T., Allouhi A., Kousksou T., Jamil A., Zeraouli Y.: *Energy and parametric analysis of solar absorption cooling systems in various Moroccan climates*. Case Stud. Therm. Eng. **9**(2017), 28–39. doi: [10.1016/j.csite.2016.11.002](https://doi.org/10.1016/j.csite.2016.11.002)
- [14] Rosen M.A., Tang R., Dincer I.: *Effect of stratification on energy and exergy capacities in thermal storage systems*. Int. J. Energy Res. **28**(2004), 177–193. doi: [10.1002/er.960](https://doi.org/10.1002/er.960)
- [15] Zhang C., Chai D., Pan X., Xie J., Chen J.: *Performance Analysis of Two Systems Combining Heat Pump and Water Vapor Compression for Waste Heat Recovery*. Appl. Sci. **12**(2022), 12853. doi: [10.3390/app122412853](https://doi.org/10.3390/app122412853)
- [16] *Heat Storage – Types of Storage* (in Polish). <https://www.cire.pl/artykuly/materialy-problemowe/119630-magazynowanie-ciepla-rodzaje-magazynow> (accessed 3 Feb. 2023).
- [17] Portarapillo M., Danzi E., Sanchirico R., Marmo L., Di Benedetto A.: *Energy recovery from winery waste: Dust explosion issues*. Appl. Sci. **11**(2021). doi: [10.3390/app112311188](https://doi.org/10.3390/app112311188)
- [18] Ugur B.: *Thermal Energy Storage in Adsorbent Beds*. PhD thesis, Univ. of Ottawa, 2013.
- [19] Shigeishi R.A., Langford C.H., Hollebone B.R.: *Solar energy storage using chemical potential changes associated with drying of zeolites*. Sol. Energy **23**(1979), 489–495. doi: [10.1016/0038-092X\(79\)90072-0](https://doi.org/10.1016/0038-092X(79)90072-0)
- [20] Badyda K., Bujalski W., Niewiński G., Warchoń M.: *Selected issues related to heat storage tank modelling and optimisation aimed at forecasting its operation*. Arch. Thermodyn. **32**(2011), 3, 3–31. doi: [10.2478/v10173-011-0010-8](https://doi.org/10.2478/v10173-011-0010-8)
- [21] Ziębik A., Gładysz P.: *Optimal coefficient of the share of cogeneration in the district heating system cooperating with thermal storage*. Arch. Thermodyn, **32**(2011), 3, 71–87. doi: [10.2478/v10173-011-0014-4](https://doi.org/10.2478/v10173-011-0014-4)

- [22] Zhu C., Zhang J., Wang Y., Deng Z., Shi P., Wu J., Wu Z.: *Study on thermal performance of single-tank thermal energy storage system with thermocline in solar thermal utilization*. Appl. Sci. **12**(2022), 3908. doi: [10.3390/app12083908](https://doi.org/10.3390/app12083908)
- [23] Szajding A., Kuta M., Cebo-Rudnicka A., Rywotycki M.: *Analysis of work of a thermal energy storage with a phase change material (PCM) charged with electric heaters from a photovoltaic installation*. Int. Commun. **140**(2023), 106547. doi: [10.1016/j.icheatmasstransfer.2022.106547](https://doi.org/10.1016/j.icheatmasstransfer.2022.106547)
- [24] Kącki E.: *Partial Differential Equations in Physics and Engineering*. WNT, Warsaw 1992 (in Polish).
- [25] Malczewski J.: *Models of Mass, Momentum and Energy Transport Processes*. PWN, Warsaw 1992 (in Polish).
- [26] Prywer J., Zarzycki R., Orzechowski Z.: *Fluid Mechanics in Environmental Engineering*. WNT, Warsaw 2001 (in Polish).
- [27] *ANSYS Manual*. ANSYS Inc. Canonsburg 2022.
- [28] Regulski W.: *Computer modeling of turbulent flows*. [https://www.meil.pw.edu.pl/za/content/download/18385/99605/file/Lab\\_67.pdf](https://www.meil.pw.edu.pl/za/content/download/18385/99605/file/Lab_67.pdf) (accessed 3 Feb. 2023)
- [29] *K-Epsilon*. <https://www.simscale.com/docs/simulation-setup/global-settings/k-epsilon/> (accessed 3 Feb. 2023).
- [30] Paszko M., Łygas K.: *Modern methods of modeling turbulent flows in the environment of a moving city bus*. <http://yadda.icm.edu.pl/baztech/element/bwmeta1.element.baztech-86cf1eb6-09ab-40e4-b9a9-9f5fb64c9e0f> (accessed 3 Feb. 2023).
- [31] *ANSYS Fluent Manual*. ANSYS Inc. Canonsburg 2022.
- [32] *ANSYS Mesh Methods Explained*. <https://featips.com/2022/12/27/ansys-mesh-methods-explained/> (accessed 3 Feb. 2023).
- [33] *How to Verify Mesh Quality in ANSYS Workbench*. <https://featips.com/2021/05/07/how-to-verify-mesh-quality-in-ansys-workbench/> (accessed 3 Feb. 2023).